INORGANIC CHEMISTRY FRONTIERS

RESEARCH ARTICLE

View Article Online
View Journal | View Issue

Cite this: *Inorg. Chem. Front.*, 2023, **10**, 4526

A strong metal–support interaction strategy for enhanced binder-free electrocatalytic nitrate reduction†

Hongxia Luo, Chuqi Wang, Jiaqiao Wang, Yuanyuan Ma* and Jianping Yang *

Received 29th April 2023,
Accepted 17th June 2023

DOI: 10.1039/d3qi00793f

rsc.li/frontiers-inorganic

An electrocatalytic nitrate reduction reaction (NO_3RR) is an attractive strategy to maintain the nitrogen neutral. Fe nanoparticles (Fe NPs) are among the most promising electrocatalysts for the NO_3RR with low cost and high performance. However, the durability of Fe-based catalysts is poor owing to the aggregation and oxidation of iron. Herein, a series of self-supported Fe/support catalysts has been synthesized by a simple hydrothermal and *in situ* thermal reduction strategy, exhibiting strong metal–support interaction (SMSI) between Fe active sites and supports. Remarkably, the iron nanoparticles loaded on graphite felt (Fe/GF) exhibited an optimal electrochemical NO_3RR performance with NO_3^- conversion of 67.7% and N_2 selectivity of 96.6%, which is attributed to the enhanced dispersity and conductivity. This study not only provides a universal method for SMSI composite catalysts but also lays the foundation for their large-scale application.

Introduction

The nitrogen neutralization cycle is an integral part of the Earth's ecosystem.[1] In recent years, excess nitrate (NO_3^-), caused by animal manure, nitrogen fertilizers and fossil fuels, has become a nitrogenous pollutant widely found in wastewater.[2,3] According to the World Health Organization (WHO) recommendations, the concentration of NO_3^- (or NO_3^-–N) in drinking water should be below 50 mg L^{-1} (or 11.3 mg L^{-1}), otherwise it may cause a serious health risk to aquatic plants and humans.[4–6] Nowadays, there are two major objectives for nitrate conversion, which are reducing the nitrates to ammonia (NH_4^+) or nitrogen (N_2).[7] Compared with the N_2 reduction reaction (N_2RR), the electrocatalytic NO_3RR for NH_4^+ production has more attractive advantages. Direct N_2RR usually exhibits low yields and Faraday efficiency due to the high dissociation energy of the strong N≡N bond (941 kJ mol^{-1}), low N_2 solubility, and competitive hydrogen evolution reaction (HER). On the other hand, NO_3^-, which has a low dissociation energy of the N–O bond (204 kJ mol^{-1}), is a common source of nitrogen and is commonly found in contaminated wastewater. As a result, the electrocatalytic NO_3RR is considered a highly effective alternative to the Haber–Bosch process.[8] However, from an environmental perspective, benign N_2 is the most promising product due to its harmless and eco-friendly characteristics.[9–11] Among the various NO_3^- treatment technologies, the electrocatalytic NO_3^- reduction reaction (NO_3RR) is considered to be the superior method for nitrate reduction in water because of the simple operation, lack of secondary pollution and environmental friendliness.[12–15]

Based on previous research studies, bimetallic-based catalysts containing noble metals (*e.g.*, Pt–Ru, Pd–Cu, Pd–Sn) are considered to be excellent catalysts for the electrocatalytic NO_3RR.[16–20] However, in order to reduce the cost and enhance the properties, numerous non-precious metal catalysts have been studied.[21–25] Fe-based electrocatalysts have stood out in replacing traditional noble metals due to their low cost, high reduction capacity, easy availability and recyclability.[26–29] However, the Fe-based nanoparticles are prone to being aggregated and oxidated.[30] To solve these problems, various strategies have been developed to improve the stability of Fe-based catalysts.[31–33] Among them, the loading strategy is deemed energetically feasible.[34–36] However, it is still a challenge to obtain uniformly dispersed iron-based nanoparticles on support without agglomeration. As is known to all, support is one of the key components of the catalyst. The catalyst supports commonly used for electrocatalysis can be classified into carbon-based supports and metal-based supports, such as active carbon, graphene, carbon nanofiber, titanium oxide, nickel foam, *etc.*[37–40] The main purpose of the support is to improve the dispersity of catalyst particles and thus enhance the catalytic performance. On the other hand, there is a

State Key Laboratory for Modification of Chemical Fibers and Polymer Materials, College of Materials Science and Engineering, Donghua University, Shanghai 201620, China. E-mail: yyma@dhu.edu.cn, jianpingyang@dhu.edu.cn

†Electronic supplementary information (ESI) available: Experimental section and ESI figures. See DOI: https://doi.org/10.1039/d3qi00793f

mutual transfer of interfacial charges between the support and the metal sites, forming a strong metal–support interaction (SMSI), which in turn affects the catalytic performance.[41] SMSI can improve the migration agglomeration of metal nanoparticles during high-temperature treatment to a certain extent, and also promote the charge transfer between the metal and the support. This strong interaction can affect the adsorption energy of reaction intermediates and thus change the catalytic performance, which is important for catalysis.[42,43] Tauster *et al.* first demonstrated the classical SMSI to solve the agglomeration problem of catalyst materials under high temperature sintering in the 1970s.[44] It is worth noting that the aggregation of iron nanostructures and the insufficient exposure of active sites caused by high surface magnetism can be effectively addressed through the SMSI between Fe active sites and support materials.[45,46]

In this work, we developed a universal strategy that can load Fe NPs on the surface of a series of carbon-based or metal-based supports (such as graphite felt (GF), carbon cloth (CC), carbon paper (CP), copper foam (CF), nickel foam (NF), and iron foam (IF)) to obtain self-supported Fe/support catalysts. The strong interaction between Fe NPs and GF is conducive to increasing the exposure of iron active sites and stability, which shows high electrocatalytic NO_3RR performance with a 67.7% NO_3^- conversion rate and a 96.6% N_2 selectivity. Besides, the performance of other Fe/support catalysts was also investigated, which showed better NO_3RR performance compared with pure carbon or metal supports. These further demonstrated that SMSI played an important role in the electrocatalytic NO_3RR and verified the favourable generalizability of this method.

Results and discussion

Fig. 1a shows the synthesis process of Fe NPs supported on carbon or metal supports. First, the treated supports were placed in an aqueous solution containing anhydrous ferric chloride ($FeCl_3$) and sodium nitrate ($NaNO_3$) and then transferred to 100 mL Teflon-lined autoclaves for a 4-hour hydrothermal reaction. Afterwards, the reacted supports were washed and dried, and then subjected to high-temperature thermal reduction treatment to obtain Fe/support catalysts (*i.e.*, Fe/GF, Fe/CC, Fe/CP, Fe/NF, Fe/CF, Fe/IF). In order to explore the optimal calcination reduction temperature, we directly synthesized the hydroxyl iron oxide (FeOOH) by the hydrothermal method (Fig. S1 and S2†) and calcined it at different temperatures. It can be concluded that when the temperature was 500 °C, the FeOOH powder still maintained a more dispersed structure and was completely reduced to Fe NPs (Fig. S3b†). However, when the temperature was 400 °C, although its structure was still maintained (Fig. S3a†), it was not completely reduced to Fe NPs. It is well known that the presence of an iron oxide mixture is not conducive to the electroreduction of NO_3^-.[47] When the temperature was higher than 500 °C, the whole structure was seriously agglomerated,

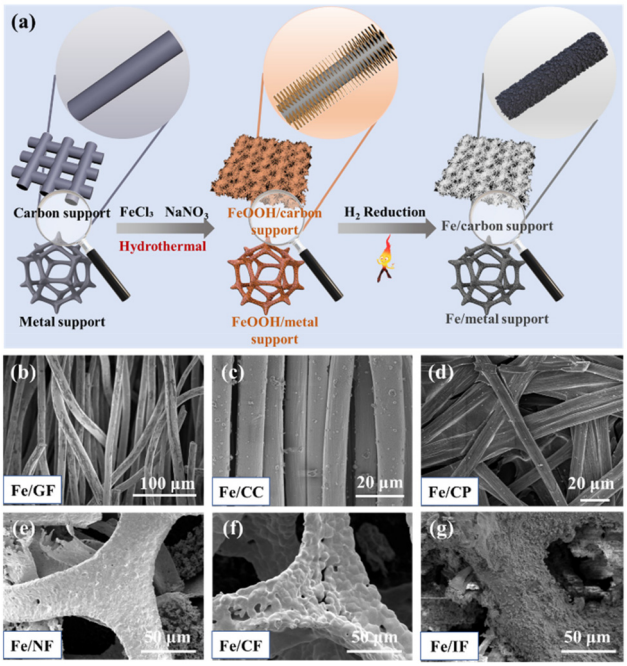

Fig. 1 (a) Schematic diagram of the synthesis of *in situ* loaded needle-like iron on carbon or metal supports. SEM images for (b) Fe/GF, (c) Fe/CC, (d) Fe/CP, (e) Fe/NF, (f) Fe/CF, and (g) Fe/IF.

resulting in a decrease in the active specific surface area, which was not suitable for the electrocatalytic NO_3RR (Fig. S3c†). Therefore, the thermal reduction temperature is fixed at 500 °C for the FeOOH on different supports to achieve the optimal structure and activity of the catalyst material. In addition, in order to verify the universality of this method, we also analyzed the morphologies corresponding to the *in situ* growth of Fe NPs in these supports. Fig. 1b–d show the *in situ* growth of Fe NPs on carbon supports. Fig. 1e–g show the *in situ* growth of Fe NPs on the metal supports. When the supports were replaced with CC and CP (Fig. S6 and S7†), the FeOOH still maintained a similar morphology, and after the thermal reduction treatment, Fe was dispersed on the carbon supports in the form of nanoparticles. On the metal supports, the smooth metal skeletons became rough, and FeOOH/NF, FeOOH/CF, and FeOOH/IF were successfully prepared (Fig. S8–S10†). After the thermal reduction, the Fe exists on the surface of the metal supports in the form of bigger particles or large bulk. It can be concluded that the catalysts maintain a complete structure in both carbon and metal supports. It is worth mentioning that the Fe NPs are relatively uniformly dispersed and anchored on the GF compared to other supports. In addition, GF exhibits a wide source and excellent electrical conductivity, and the GF itself has the effect of NO_3^- accumulation, which may further improve the conversion rate of NO_3^- in the electrolyte.[48] Furthermore, compared with metal supports, carbon-based supports exhibit excellent corrosion and oxidation resistance. Therefore, the following research will focus on the Fe/GF catalyst for an in-depth discussion.

Needle-like FeOOH was *in situ* grown on hydrophilic GF *via* a one-step method and then calcined at 500 °C under an H_2/Ar atmosphere to obtain the Fe/GF catalyst. Compared with pure GF support (Fig. S4†), it can be clearly observed that the ordered FeOOH vertically grows on the surface of GF and forms a uniformly distributed array (Fig. 2a–c). The SEM images of the Fe/GF catalyst are shown in Fig. 2d–f. In addition, we also performed TEM tests for Fe/GF and found that the iron nanoparticles had an irregular shape but a relatively uniform particle size (Fig. S5†). The EDS elemental mapping images (Fig. 2g) show that the Fe element is uniformly distributed on GF. To further explore the precise structure and composition of the material, the Fe/GF-*X* (*X* = 400 and 600, which means the reduction temperature) catalysts were investigated by powder X-ray diffraction (PXRD). As shown in Fig. 2h, the diffraction peaks of Fe/GF-400 can be attributed to the composite structure of Fe (JCPDS no. 06-0696) and Fe_3O_4 (JCPDS no. 19-0629). The diffraction peaks of Fe/GF and Fe/GF-600 at 44.7°, 65.0° and 82.3° were ascribed to the crystalline surface of Fe (JCPDS no. 06-0696).[47] This result indicated that the Fe/GF self-support electrocatalyst was successfully prepared at a thermal reduction temperature under 500 °C. In addition, the degree of graphitization of Fe/GF was characterized by Raman spectroscopy (Fig. 2i). The intensity ratios of the D band to G band (I_D/I_G) of these catalysts are all around 0.88, suggesting the high graphitization of carbon supports, which could provide a high level of electrochemical conductivity.[49] Further analysis by XPS shows that the catalyst is mainly composed of Fe, C, and O elements (Fig. S11(a)†). The Fe 2p spectrum shows that the material is composed of zero-valent Fe and Fe^{2+} and Fe^{3+}, where the Fe oxides are derived from the surface oxidation of zero-valent Fe nanoparticles (Fig. S11(b)†).

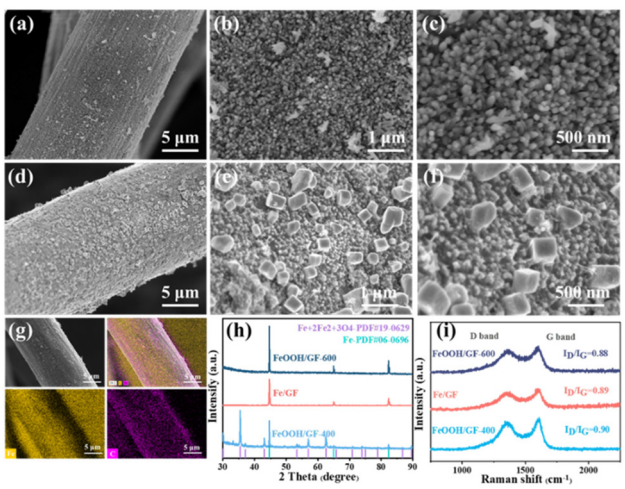

Fig. 2 (a–c) SEM images of FeOOH/GF, (d–f) SEM images of Fe/GF, (g) EDX mapping image and the corresponding mapping scan images, (h) XRD patterns and (i) Raman spectra of Fe/GF with different calcination temperatures.

The electrocatalytic reduction process of NO_3^- was employed in a 50 mL single-chamber electrochemical reaction cell by a typical three-electrode system. In order to eliminate the effect of the electrode on the electrocatalytic nitrate reduction of the Fe/GF catalyst, we replaced the graphite rod to perform a series of comparative experiments on the electrode. The results showed that the effect on catalyst performance was not significant when a graphite rod was used as the electrode in a neutral electrolyte (Fig. S12†).[50] We then explored the performance of all supports and Fe/support catalysts to select the optimum catalyst (Fig. 3a). It can be observed that the Fe/GF exhibits a better NO_3^- conversion rate and N_2 selectivity, which is attributed to the three-dimensional spatial network structure of GF and the excellent dispersion of Fe NPs on the surface of GF. The GF support not only enhances the conductivity of the catalyst, but also improves the utilization of the active material as well as accelerating the mass transfer of NO_3^- in the electrolyte, which contributes to the better catalytic performance of Fe/GF. Therefore, in order to investigate the effects of various factors on the electrocatalytic NO_3RR performance, we focus on Fe/GF for further analysis and discussion. Linear scanning voltammetry (LSV) tests were performed in 0.03 M Na_2SO_4 and 0.01 M NaCl electrolytes under neutral conditions to detect the electrocatalytic activity of NO_3^-. In the

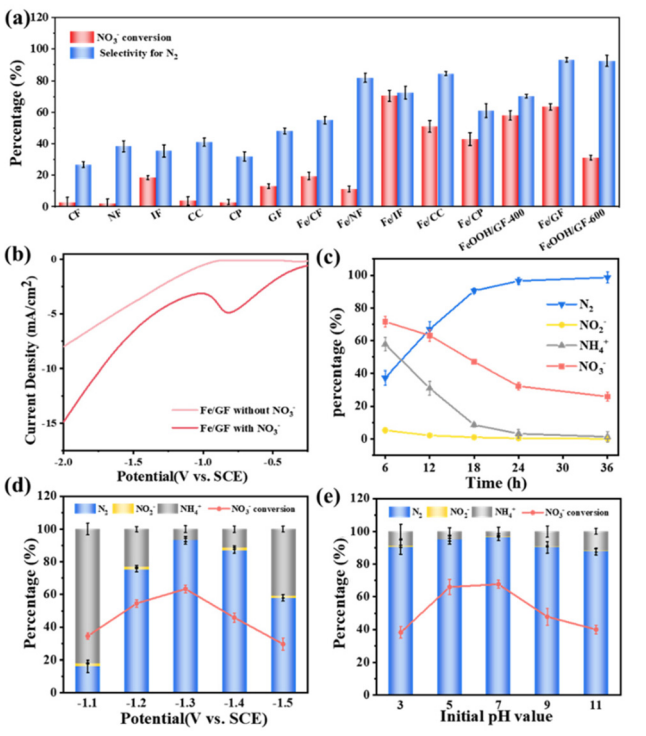

Fig. 3 (a) The performance of different catalysts under the same testing conditions. (b) LSV curves of Fe/GF in the absence and presence of 100 mg L^{-1} NO_3^-–N. (c) Nitrate conversion and selectivity of nitrogenous products of Fe/GF results along with time. Effects of (d) applied potential and (e) initial pH value on the NO_3^- conversion and N_2 selectivity of Fe/GF.

electrolyte containing 100 mg L^{-1} NO_3^-–N, the cathodic current density was increased obviously, and the reduction peak was only detected in the nitrate-containing electrolyte (Fig. 3b). The reduction peak here was attributed to the NO_3^- to NO_2^- electrocatalytic reaction.[51,52] Fig. 3c demonstrates the evolution of NO_3^-, NO_2^-, NH_4^+, and N_2 with reaction time under these conditions. As the electrolysis time increased from 6 to 24 hours, the content of NO_3^-–N gradually decreased from 71.6% to 32.3%. With the increase in reaction time, the N_2 content gradually increased owing to the consumption of NH_4^+ by the breakpoint chlorination reaction.[53] In addition, the effects of various parameter conditions were evaluated in detail, including the cathodic reduction potential, the initial pH, the initial electrolyte type, and the initial NO_3^-–N concentration. In a practical electrocatalytic NO_3RR process, the optimum applied potential is essential for the effective electrocatalytic NO_3RR to avoid the generation of harmful by-products. As shown in Fig. 3d, when the cathode potential was applied from −1.1 V to −1.3 V *vs.* SCE, the NO_3^- conversion rate could increase from 34.6% to 67.7% and the N_2 selectivity increased from 16.1% to 96.6%. This indicated that the conversion rate of NO_3^- responds well to the reduction potential and current density (Fig. S13†). However, as the reduction voltage increased to −1.5 V *vs.* SCE, the NO_3^- conversion rate and N_2 selectivity were significantly decreased to 29.6% and 57.9%, respectively. This is due to the competition for electrons by the excessive hydrogen evolution reaction and the inhibition of ion transport by the bubbles formed on the surface of the catalysts. On the other hand, the electrode itself cannot withstand excessive voltages, which can result in a significant loss of iron active sites.[54] Different initial pH values (pH = 3.0, 5.0, 7.0, 9.0, 11.0) were also carried out to analyse the electrocatalytic NO_3RR performance of Fe/GF (Fig. 3e and Fig. S14†). It is clear that the best values of NO_3^- conversion rate and N_2 selectivity are achieved at an initial pH of 7.0. In the acidic system, the generated hydrogen bubbles wrapped around the surface of the active material, hindering sufficient contact between the active sites and the electrolyte, thus slightly reducing the electrocatalytic performance. The higher pH may lead to the adsorption of hydroxide on the surface of catalysts, thus occupying the active surface, which is not favorable for electron transfer.[55] In addition, the effect of the electrolyte was further evaluated. To determine the optimal electrolyte system, different molar ratios of NaCl and Na_2SO_4 were employed to study the electrocatalytic NO_3RR (Fig. S15 and S16†). According to the "breakpoint chlorination theory", in the Cl^- containing system, the intermediate product hypochlorite produced by Cl^- can consume NH_4^+ produced near the anode surface and convert it to N_2, which is consistent with the experimental results of product distribution and is the main source of N_2 in the catalytic process.[56] In contrast, the increase in the SO_4^{2-} concentration facilitates the conversion of nitrate to NH_4^+, and the addition of an appropriate amount of SO_4^{2-} can improve the conductivity of the electrolyte and promote ion transport.[57] According to the above result, the optimal electrolyte system for the Fe/GF catalyst consisted of 0.01 M NaCl and 0.03 M Na_2SO_4, with a NO_3^- conversion rate of 67.7% and a N_2 selectivity of 96.6%. Furthermore, in the neutral system with a mixing electrolyte, the nitrate conversion was gradually enhanced when the initial NO_3^-–N concentration was increased from 20 mg L^{-1} to 100 mg L^{-1} (Fig. S17 and S18†). When the initial NO_3^-–N concentration was too low, the amount of NO_3^- was insufficient, and the interaction of the active center with NO_3^- was considerably weak. The competition between the hydrogen evolution reaction and NO_3^- adsorption may lead to a decrease in the electrocatalytic NO_3RR. When the NO_3^-–N concentration increased to 150–200 mg L^{-1}, the products of NO_3^- reduction did not easily diffuse from the surface of the active site. At the same time, it migrates to the surface of the active site with difficulty due to the unremovable NO_3^-, which leads to a decrease in the electrocatalytic nitrate reduction performance.[58] Therefore, the optimal electrolytic conditions for the Fe/GF catalyst were at −1.3 V *vs.* SCE in the initial electrolyte solution of 0.01 M NaCl, 0.03 M Na_2SO_4 and 100 mg L^{-1} NO_3^-–N concentration with a pH of 7.

Stability is another important indicator for electrocatalysts. To achieve large-scale application, a catalyst with high stability is necessary. Fig. 4a shows the electrocatalytic NO_3RR for eight replicate cycles (each cycle lasting for 24 h). It is noteworthy that the conversion rate of NO_3^- varies in the range of 58.8–67.6%, indicating the good stability and reusability of Fe/GF. The SEM image (Fig. 4b) shows that Fe nanoparticles remained attached in the GF after 8 cycles, further demonstrating its structural stability. Based on the above results, the mechanism of the electrocatalytic NO_3RR process for these Fe/support catalysts can be reasonably deduced (Fig. 4c). The

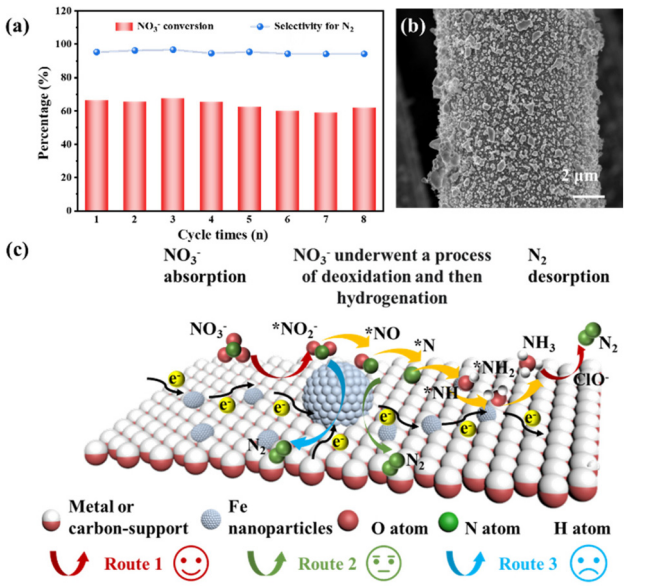

Fig. 4 (a) Nitrate conversion and nitrogen selectivity of Fe/GF during 8 repeated electrolysis tests. (b) SEM images of Fe/GF after 8 cycles. (c) Reaction mechanism diagram of Fe/metal or carbon support in the bi-electrolyte (NaCl and Na_2SO_4) system.

electrocatalytic NO_3RR is a transformation of electrons and protons (eqn (1)–(10)).[59] NO_3^- is first adsorbed on the surface of iron nanoparticles, and the 3d orbital of Fe is coupled with the 2p orbital of N (from NO_3^-) under the action of electrons; then, the N–O band is broken and converted to NO_2^- after removing an oxygen atom. Since the conversion of NO_3^- to NO_2^- requires a higher energy barrier and longer reaction time, this process is often referred to as the "rate-determining step". Fe nanoparticles continue to provide electrons to NO_2^- and further reduce it to other nitrogen-containing intermediates such as *NO. Notably, *NO is the key intermediate which determines the product selectivity. Here, the reaction process can be divided into three routes. Route 1 is the deoxidation process of NO_3^- and then gradual hydrogenation, followed by the combination of active hydrogen with electrons from the Fe active site, which may lead to the formation of N_2 or NH_4^+. In addition, according to the "breakpoint chlorination" theory, the concentration of NH_4^+ in the reaction solution gradually decreases and the content of N_2 gradually increases due to the oxidation of Cl^- at the anode to form HClO (eqn (11)–(14)). It should be noted that ClO^- could be supposed to be a reducing agent to promote the cyclic regeneration of Fe^{3+} to Fe^{2+}, providing a continuous supply of catalytic active sites for the electrocatalytic NO_3RR.[60] Route 2 acquires N_2 through the combination of the intermediate NO. In addition, due to the SMSI between supports and Fe, the excellent electrical conductivity of supports could accelerate the transfer of electrons to Fe NPs, thus promoting the rapid electroreduction of NO_3^-. In Route 3, NO_3^- first removes an oxygen to form NO_2^- intermediates and then directly reduces to N_2 under the action of electrons. Due to the high energy required to break the N≡N bond, the N_2 production by this route is very low.

$$NO_3^-(aq) \rightarrow NO_3^-(ads) \quad (1)$$

$$NO_3^-(ads) + 2H(ads) \rightarrow NO_3^-(ads) + H_2O \quad (2)$$

$$2NO_2^-(ads) + 4H_2O + 6e^- \rightarrow N_2 + 8OH^- \quad (3)$$

$$NO_2^-(ads) + H(ads) \rightarrow NO(ads) + OH^- \quad (4)$$

$$NO(ads) + 2H(ads) \rightarrow N(ads) + H_2O \quad (5)$$

$$NO(ads) + NO(ads) + 2H^+ + 2e^- \rightarrow N_2O + H_2O \quad (6)$$

$$N_2O + 2H^+ + e^- \rightarrow N_2 + H_2O \quad (7)$$

$$N(ads) + H(ads) \rightarrow NH(ads) \quad (8)$$

$$NH(ads) + H(ads) \rightarrow NH_2(ads) \quad (9)$$

$$NH_2(ads) + H(ads) \rightarrow NH_3(ads) \quad (10)$$

$$2NH_4^+ + 3ClO^- \rightarrow N_2 + 3Cl^- + 2H^+ + 3H_2O \quad (11)$$

$$2Cl^- \rightarrow Cl_2(aq) + 2e^- \quad (12)$$

$$Cl_2(aq) + H_2O \rightarrow HClO + Cl^- + H^+ \quad (13)$$

$$HClO \rightarrow ClO^- + H^+ \quad (14)$$

Conclusions

In summary, a series of self-supported Fe/support electrocatalysts containing SMSI has been prepared by a simple hydrothermal and thermal reduction process. Among them, the Fe/GF electrode has strong conductivity, a high utilization rate of active sites and fast electron transfer efficiency, showing excellent electrocatalytic nitrate removal activity. After 24 h of reaction, the NO_3^- conversion and N_2 selectivity of Fe/GF reach 67.7% and 96.6%, respectively, and it still maintains good stability after 8 cycles. It is believed that this universal synthesis method could provide ideas for the development of metal–support catalysts with high conductivity and stability. In addition, this study could further provide guidance for iron-based electrocatalysts in the field of electrocatalytic NO_3RR.

Conflicts of interest

There are no conflicts to declare.

Acknowledgements

This work was supported by the National Natural Science Foundation of China (No. 52172291, 52122312, and 22022608), "Shuguang Program" supported by the Shanghai Education Development Foundation and Shanghai Municipal Education Commission (22SG31), and the State Key Laboratory for Modification of Chemical Fibers and Polymer Materials (Donghua University).

References

1 N. Lehnert, B. W. Musselman and L. C. Seefeldt, Grand challenges in the nitrogen cycle, *Chem. Soc. Rev.*, 2021, **50**, 3640–3646.
2 S. Yuan, Y. Xue, R. Ma, Q. Ma, Y. Chen and J. Fan, Advances in iron-based electrocatalysts for nitrate reduction, *Sci. Total Environ.*, 2023, **866**, 161444.
3 X. Zhao, X. Zhao, P. Liu, D. Chen, C. Zhang, C. Xue, J. Liu, J. Xu and Y. Mu, Transport pathways of nitrate formed from nocturnal N_2O_5 hydrolysis aloft to the ground level in winter north China plain, *Environ. Sci. Technol.*, 2023, **57**, 2715–2725.
4 C. Yu, X. Huang, H. Chen, H. C. J. Godfray, J. S. Wright, J. W. Hall, P. Gong, S. Ni, S. Qiao, G. Huang, Y. Xiao, J. Zhang, Z. Feng, X. Ju, P. Ciais, N. C. Stenseth, D. O. Hessen, Z. Sun, L. Yu, W. Cai, H. Fu, X. Huang, C. Zhang, H. Liu and J. Taylor, Managing nitrogen to restore water quality in China, *Nature*, 2019, **567**, 516–520.
5 A. S. Elrys, Y. Uwiragiye, Y. Zhang, M. K. Abdel-Fattah, Z.-X. Chen, H.-M. Zhang, L. Meng, J. Wang, T.-B. Zhu, Y. Cheng, J.-B. Zhang, Z.-C. Cai, S. X. Chang and C. Müller, Expanding agroforestry can increase nitrate retention and

mitigate the global impact of a leaky nitrogen cycle in croplands, *Nat. Food*, 2023, **4**, 109–121.

6 L. Lin, S. St Clair, G. D. Gamble, C. A. Crowther, L. Dixon, F. H. Bloomfield and J. E. Harding, Nitrate contamination in drinking water and adverse reproductive and birth outcomes: a systematic review and meta-analysis, *Sci. Rep.*, 2023, **13**, 563.

7 T. Wu, P. Wang and Y. Zhang, Microenvironment optimization towards electrocatalytic ammonia synthesis: recent progress and future, *Mater. Lab.*, 2022, **1**, 220011.

8 H. Jiang, G.-F. Chen, O. Savateev, J. Xue, L.-X. Ding, Z. Liang, M. Antonietti and H. Wang, Enabled efficient ammonia synthesis and energy supply in a zinc-nitrate battery system by separating nitrate reduction process into two stages, *Angew. Chem., Int. Ed.*, 2023, **62**, e202218717.

9 S. Lee, Y. Lee and W. Choi, Direct photoconversion of nitrite to dinitrogen on Pd/TiO_2 coupled with photooxidation of aquatic pollutants, *Appl. Catal., B*, 2023, **327**, 122432.

10 X. Wang, X. Wu, W. Ma, X. Zhou, S. Zhang, D. Huang, L. R. Winter, J.-H. Kim and M. Elimelech, Free-standing membrane incorporating single-atom catalysts for ultrafast electroreduction of low-concentration nitrate, *Proc. Natl. Acad. Sci. U. S. A.*, 2023, **120**, e2217703120.

11 K. Fan, W. Xie, J. Li, Y. Sun, P. Xu, Y. Tang, Z. Li and M. Shao, Active hydrogen boosts electrochemical nitrate reduction to ammonia, *Nat. Commun.*, 2022, **13**, 7958.

12 Y. Bai, S. Wang, A. Zhussupbekova, I. V. Shvets, P.-H. Lee and X. Zhan, High-rate iron sulfide and sulfur-coupled autotrophic denitrification system: Nutrients removal performance and microbial characterization, *Water Res.*, 2023, **231**, 119619.

13 B. Li, F. Xia, Y. Liu, H. Tan, S. Gao, J. Kaelin, Y. Liu, K. Lu, T. J. Marks and Y. Cheng, $Co_2Mo_6S_8$ catalyzes nearly exclusive electrochemical nitrate conversion to ammonia with enzyme-like activity, *Nano Lett.*, 2023, **23**, 1459–1466.

14 Y. Luo, K. Chen, G. Wang, G. Zhang, N. Zhang and K. Chu, Ce-doped MoS_{2-x} nanoflower arrays for electrocatalytic nitrate reduction to ammonia, *Inorg. Chem. Front.*, 2023, **10**, 1543–1551.

15 H. Xu, J. Chen, Z. Zhang, C.-T. Hung, J. Yang and W. Li, In situ confinement of ultrasmall metal nanoparticles in short mesochannels for durable electrocatalytic nitrate reduction with high efficiency and selectivity, *Adv. Mater.*, 2023, **35**, 2207522.

16 L. Sun and B. Liu, Mesoporous PdN alloy nanocubes for efficient electrochemical nitrate reduction to ammonia, *Adv. Mater.*, 2023, **35**, 2207305.

17 H. Liu, J. Timoshenko, L. Bai, Q. Li, M. Rüscher, C. Sun, B. Roldan Cuenya and J. Luo, Low-coordination rhodium catalysts for an efficient electrochemical nitrate reduction to ammonia, *ACS Catal.*, 2023, **13**, 1513–1521.

18 D. Chen, S. Zhang, D. Yin, W. Li, X. Bu, Q. Quan, Z. Lai, W. Wang, Y. Meng, C. Liu, S. Yip, F.-R. Chen, C. Zhi and J. C. Ho, Tailored p-orbital delocalization by diatomic Pt–Ce induced interlayer spacing engineering for highly-efficient ammonia electrosynthesis, *Adv. Energy Mater.*, 2023, **13**, 2203201.

19 X. Li, P. Shen, X. Li, D. Ma and K. Chu, Sub-nm RuO_x clusters on Pd metallene for synergistically enhanced nitrate electroreduction to ammonia, *ACS Nano*, 2023, **17**, 1081–1090.

20 X. Zhao, Y. Cao, L. Duan, R. Yang, Z. Jiang, C. Tian, S. Chen, X. Duan, D. Chen and Y. Wan, Unleash electron transfer in C–H functionalization by mesoporous carbon-supported palladium interstitial catalysts, *Natl. Sci. Rev.*, 2021, **8**, nwaa126.

21 T. Li, C. Tang, H. Guo, H. Wu, C. Duan, H. Wang, F. Zhang, Y. Cao, G. Yang and Y. Zhou, In situ growth of Fe_2O_3 nanorod arrays on carbon cloth with rapid charge transfer for efficient nitrate electroreduction to ammonia, *ACS Appl. Mater. Interfaces*, 2022, **14**, 49765–49773.

22 Q. Liu, Q. Liu, L. Xie, Y. Ji, T. Li, B. Zhang, N. Li, B. Tang, Y. Liu, S. Gao, Y. Luo, L. Yu, Q. Kong and X. Sun, High-performance electrochemical nitrate reduction to ammonia under ambient conditions using a FeOOH nanorod catalyst, *ACS Appl. Mater. Interfaces*, 2022, **14**, 17312–17318.

23 X. He, J. Li, R. Li, D. Zhao, L. Zhang, X. Ji, X. Fan, J. Chen, Y. Wang, Y. Luo, D. Zheng, L. Xie, S. Sun, Z. Cai, Q. Liu, K. Ma and X. Sun, Ambient ammonia synthesis via nitrate electroreduction in neutral media on Fe_3O_4 nanoparticles-decorated TiO_2 nanoribbon array, *Inorg. Chem.*, 2023, **62**, 25–29.

24 C. Wang, P. Zhai, M. Xia, W. Liu, J. Gao, L. Sun and J. Hou, Identification of the origin for reconstructed active sites on oxyhydroxide for oxygen evolution reaction, *Adv. Mater.*, 2023, **35**, 2209307.

25 W. Duan, Y. Chen, H. Ma, J.-F. Lee, Y.-J. Lin and C. Feng, In situ reconstruction of metal oxide cathodes for ammonium generation from high-strength nitrate wastewater: Elucidating the role of the substrate in the performance of Co_3O_{4-x}, *Environ. Sci. Technol.*, 2023, **57**, 3893–3904.

26 J. Zhao, L. Liu, Y. Yang, D. Liu, X. Peng, S. Liang and L. Jiang, Insights into electrocatalytic nitrate reduction to ammonia via Cu-based bimetallic catalysts, *ACS Sustainable Chem. Eng.*, 2023, **11**, 2468–2475.

27 J.-X. Liu, D. Richards, N. Singh and B. R. Goldsmith, Activity and selectivity trends in electrocatalytic nitrate reduction on transition metals, *ACS Catal.*, 2019, **9**, 7052–7064.

28 G. Zhang, X. Li, K. Chen, Y. Guo, D. Ma and K. Chu, Tandem electrocatalytic nitrate reduction to ammonia on MBenes, *Angew. Chem., Int. Ed.*, 2023, **62**, e202300054.

29 M. Cai, Q. Zhu, X. Wang, Z. Shao, L. Yao, H. Zeng, X. Wu, J. Chen, K. Huang and S. Feng, Formation and stabilization of NiOOH by introducing α-FeOOH in LDH: Composite electrocatalyst for oxygen evolution and urea oxidation reactions, *Adv. Mater.*, 2023, **35**, 2209338.

30 H.-W. Zheng, X.-Y. Shu, Y. Li and J.-P. Zhao, Mechanical properties of Fe-based amorphous–crystalline composite: A molecular dynamics simulation and experimental study, *Rare Met.*, 2021, **40**, 2560–2567.

31 H. Zhang, C. Wang, H. Luo, J. Chen, M. Kuang and J. Yang, Iron nanoparticles protected by chainmail-structured graphene for durable electrocatalytic nitrate reduction to nitrogen, *Angew. Chem., Int. Ed.*, 2023, **62**, e202217071.

32 C. Q. Wang, Y. B. Zhang, H. X. Luo, H. Zhang, W. Li, W.-x. Zhang and J. P. Yang, Iron-based nanocatalysts for electrochemical nitrate reduction, *Small Methods*, 2022, **6**, 2200790.

33 T. Xu, J. Liang, Y. Wang, S. Li, Z. Du, T. Li, Q. Liu, Y. Luo, F. Zhang, X. Shi, B. Tang, Q. Kong, A. M. Asiri, C. Yang, D. Ma and X. Sun, Enhancing electrocatalytic N_2-to-NH_3 fixation by suppressing hydrogen evolution with alkylthiols modified Fe_3P nanoarrays, *Nano Res.*, 2022, **15**, 1039–1046.

34 L.-S. Zhang, X.-H. Jiang, Z.-A. Zhong, L. Tian, Q. Sun, Y.-T. Cui, X. Lu, J.-P. Zou and S.-L. Luo, Carbon nitride supported high-lloading Fe single-atom catalyst for activation of peroxymonosulfate to generate $^1O_2$ with 100% selectivity, *Angew. Chem., Int. Ed.*, 2021, **60**, 21751–21755.

35 Z. He, J. Zhang, Z. Gong, H. Lei, D. Zhou, N. Zhang, W. Mai, S. Zhao and Y. Chen, Activating lattice oxygen in NiFe-based (oxy)hydroxide for water electrolysis, *Nat. Commun.*, 2022, **13**, 2191.

36 X. Zhao, Y. Cao, L. Duan, R. Yang, Z. Jiang, C. Tian, S. Chen, X. Duan, D. Chen and Y. Wan, Unleash electron transfer in C–H functionalization by mesoporous carbon-supported palladium interstitial catalysts, *Natl. Sci. Rev.*, 2021, **8**, nwaa126.

37 F.-Y. Chen, Z.-Y. Wu, S. Gupta, D. J. Rivera, S. V. Lambeets, S. Pecaut, J. Y. T. Kim, P. Zhu, Y. Z. Finfrock, D. M. Meira, G. King, G. Gao, W. Xu, D. A. Cullen, H. Zhou, Y. Han, D. E. Perea, C. L. Muhich and H. Wang, Efficient conversion of low-concentration nitrate sources into ammonia on a Ru-dispersed Cu nanowire electrocatalyst, *Nat. Nanotechnol.*, 2022, **17**, 759–767.

38 X. Chen, T. Zhang, M. Kan, D. Song, J. Jia, Y. Zhao and X. Qian, Binderless and oxygen vacancies rich FeNi/graphitized mesoporous carbon/Ni foam for electrocatalytic reduction of nitrate, *Environ. Sci. Technol.*, 2020, **54**, 13344–13353.

39 J. Ge, S. Diao, J. Jin, Y. Wang, X. Zhao, F. Zhang and X. Lei, NiFeCu phosphides with surface reconstruction via the topotactic transformation of layered double hydroxides for overall water splitting, *Inorg. Chem. Front.*, 2023, **10**, 3515–3524.

40 F. Zhang, J. Chen and J. Yang, Fiber materials for electrocatalysis applications, *Adv. Fiber Mater.*, 2022, **4**, 720–735.

41 T. W. van Deelen, C. Hernández Mejía and K. P. de Jong, Control of metal-support interactions in heterogeneous catalysts to enhance activity and selectivity, *Nat. Catal.*, 2019, **2**, 955–970.

42 Q.-Q. Yan, D.-X. Wu, S.-Q. Chu, Z.-Q. Chen, Y. Lin, M.-X. Chen, J. Zhang, X.-J. Wu and H.-W. Liang, Reversing the charge transfer between platinum and sulfur-doped carbon support for electrocatalytic hydrogen evolution, *Nat. Commun.*, 2019, **10**, 4977.

43 W. Qiu, M. Xie, P. Wang, T. Gao, R. Li, D. Xiao, Z. Jin and P. Li, Size-defined Ru nanoclusters supported by TiO_2 nanotubes enable low-concentration nitrate electroreduction to ammonia with suppressed hydrogen evolution, *Small*, 2023, 2300437.

44 S. J. Tauster, S. C. Fung and R. L. Garten, Strong metal-support interactions. Group 8 noble metals supported on titanium dioxide, *J. Am. Chem. Soc.*, 1978, **100**, 170–175.

45 R. Belgamwar, R. Verma, T. Das, S. Chakraborty, P. Sarawade and V. Polshettiwar, Defects tune the strong metal–support interactions in copper supported on defected titanium dioxide catalysts for CO_2 reduction, *J. Am. Chem. Soc.*, 2023, **145**, 8634–8646.

46 G. Wu, Y. Liu and J. Wang, Oxidative-atmosphere-induced strong metal–support interaction and its catalytic application, *Acc. Chem. Res.*, 2023, **56**, 911–923.

47 Y. Lan, J. Chen, H. Zhang, W.-X. Zhang and J. Yang, Fe/Fe_3C nanoparticle-decorated N-doped carbon nanofibers for improving the nitrogen selectivity of electrocatalytic nitrate reduction, *J. Mater. Chem. A*, 2020, **8**, 15853–15863.

48 J. Chen, K. Zuo, Y. Li, X. Huang, J. Hu, Y. Yang, W. Wang, L. Chen, A. Jain, R. Verduzco, X. Li and Q. Li, Eggshell membrane derived nitrogen rich porous carbon for selective electrosorption of nitrate from water, *Water Res.*, 2022, **216**, 118351.

49 X. Wang, H. Huang, J. Qian, Y. Li and K. Shen, Intensified Kirkendall effect assisted construction of double-shell hollow Cu-doped CoP nanoparticles anchored by carbon arrays for water splitting, *Appl. Catal., B*, 2023, **325**, 122295.

50 Y.-T. Xu, X. Xiao, Z.-M. Ye, S. Zhao, R. Shen, C.-T. He, J.-P. Zhang, Y. Li and X.-M. Chen, Cage-confinement pyrolysis route to ultrasmall tungsten carbide nanoparticles for efficient electrocatalytic hydrogen evolution, *J. Am. Chem. Soc.*, 2017, **139**, 5285–5288.

51 H. Yin, Y. Peng and J. Li, Electrocatalytic reduction of nitrate to ammonia via a Au/Cu single atom alloy catalyst, *Environ. Sci. Technol.*, 2023, **57**, 3134–3144.

52 Z. Fang, Z. Jin, S. Tang, P. Li, P. Wu and G. Yu, Porous two-dimensional iron-cyano nanosheets for high-rate electrochemical nitrate reduction, *ACS Nano*, 2022, **16**, 1072–1081.

53 Y. Lan, H. Luo, Y. Ma, Y. Hua, T. Liao and J. Yang, Synergy between copper and iron sites inside carbon nanofibers for superior electrocatalytic denitrification, *Nanoscale*, 2021, **13**, 10108–10115.

54 J. Wang, D. Wu, M. Li, X. Wei, X. Yang, M. Shao and M. Gu, Bismuth ferrite as an electrocatalyst for the electrochemical nitrate reduction, *Nano Lett.*, 2022, **22**, 5600–5606.

55 K. Wang, R. Mao, R. Liu, J. Zhang and X. Zhao, Sulfur-dopant-promoted electrocatalytic reduction of nitrate by a self-supported iron cathode: Selectivity, stability, and underlying mechanism, *Appl. Catal., B*, 2022, **319**, 121862.

56 J. Zhou, F. Pan, Q. Yao, Y. Zhu, H. Ma, J. Niu and J. Xie, Achieving efficient and stable electrochemical nitrate removal by *in situ* reconstruction of Cu_2O/Cu electroactive nanocatalysts on Cu foam, *Appl. Catal., B*, 2022, **317**, 121811.

57 L. Su, D. Han, G. Zhu, H. Xu, W. Luo, L. Wang, W. Jiang, A. Dong and J. Yang, Tailoring the assembly of iron nanoparticles in carbon microspheres toward high-performance electrocatalytic denitrification, *Nano Lett.*, 2019, **19**, 5423–5430.

58 Z. Song, Y. Liu, Y. Zhong, Q. Guo, J. Zeng and Z. Geng, Efficient electroreduction of nitrate into ammonia at ultralow concentrations via an enrichment effect, *Adv. Mater.*, 2022, **34**, 2204306.

59 Q. Zhao, Z. Tang, B. Chen, C. Zhu, H. Tang and G. Meng, Efficient electrocatalytic reduction of nitrate to nitrogen gas by a cubic Cu_2O film with predominant (111) orientation, *Chem. Commun.*, 2022, **58**, 3613–3616.

60 J. Wang, Z. Deng, T. Feng, J. Fan and W.-x. Zhang, Nanoscale zero-valent iron (nZVI) encapsulated within tubular nitride carbon for highly selective and stable electrocatalytic denitrification, *Chem. Eng. J.*, 2021, **417**, 129160.